

Lawrence Berkeley National Laboratory

LBL Publications

Title

Faster Crystallization during Coral Skeleton Formation Correlates with Resilience to Ocean Acidification

Permalink

<https://escholarship.org/uc/item/8sg0h162>

Journal

Journal of the American Chemical Society, 144(3)

ISSN

0002-7863

Authors

Schmidt, Connor A

Stifler, Cayla A

Luffey, Emily L

et al.

Publication Date

2022-01-26

DOI

10.1021/jacs.1c11434

Peer reviewed

Faster Crystallization during Coral Skeleton Formation Correlates with Resilience to Ocean Acidification

Connor A. Schmidt, Cayla A. Stifler, Emily L. Luffey, Benjamin I. Fordyce, Asiya Ahmed, Gabriela Barreiro Pujol, Carolyn P. Breit, Sydney S. Davison, Connor N. Klaus, Isaac J. Koehler, Isabelle M. LeCloux, Celeo Matute Diaz, Catherine M. Nguyen, Virginia Quach, Jaden S. Sengkhamee, Evan J. Walch, Max M. Xiong, Eric Tambutté, Sylvie Tambutté, Tali Mass, and Pupa U. P. A. Gilbert*

Cite This: *J. Am. Chem. Soc.* 2022, 144, 1332–1341

Read Online

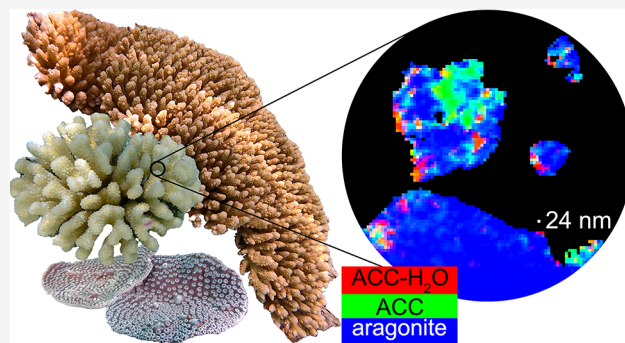
ACCESS |

Metrics & More

Article Recommendations

Supporting Information

ABSTRACT: The mature skeletons of hard corals, termed stony or scleractinian corals, are made of aragonite (CaCO_3). During their formation, particles attaching to the skeleton's growing surface are calcium carbonate, transiently amorphous. Here we show that amorphous particles are observed frequently and reproducibly just outside the skeleton, where a calcicoblastic cell layer envelops and deposits the forming skeleton. The observation of particles in these locations, therefore, is consistent with nucleation and growth of particles in intracellular vesicles. The observed extraskeletal particles range in size between 0.2 and 1.0 μm and contain more of the amorphous precursor phases than the skeleton surface or bulk, where they gradually crystallize to aragonite. This observation was repeated in three diverse genera of corals, *Acropora* sp., *Stylophora pistillata*—differently sensitive to ocean acidification (OA)—and *Turbinaria peltata*, demonstrating that intracellular particles are a major source of material during the additive manufacturing of coral skeletons. Thus, particles are formed away from seawater, in a presumed intracellular calcifying fluid (ICF) in closed vesicles and not, as previously assumed, in the extracellular calcifying fluid (ECF), which, unlike ICF, is partly open to seawater. After particle attachment, the growing skeleton surface remains exposed to ECF, and, remarkably, its crystallization rate varies significantly across genera. The skeleton surface layers containing amorphous pixels vary in thickness across genera: $\sim 2.1 \mu\text{m}$ in *Acropora*, $1.1 \mu\text{m}$ in *Stylophora*, and $0.9 \mu\text{m}$ in *Turbinaria*. Thus, the slow-crystallizing *Acropora* skeleton surface remains amorphous and soluble longer, including overnight, when the pH in the ECF drops. Increased skeleton surface solubility is consistent with *Acropora*'s vulnerability to OA, whereas the *Stylophora* skeleton surface crystallizes faster, consistent with *Stylophora*'s resilience to OA. *Turbinaria*, whose response to OA has not yet been tested, is expected to be even more resilient than *Stylophora*, based on the present data.



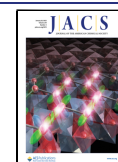
INTRODUCTION

All scleractinian or stony corals form aragonite (CaCO_3) skeletons, which provide the scaffolding for entire coral reef ecosystems. Will coral reefs survive ocean acidification (OA)? Current models and projections include predictions that corals will continue to calcify even when water chemistry in coral reefs switches from net precipitation to net dissolution, which is expected to happen in 2050.¹ Why this is the case, however, is unclear. Importantly, different coral genera respond differently to OA.² *Stylophora pistillata*, one of the most studied coral species, exhibits the greatest resilience to OA.² *S. pistillata* was shown to form its aragonite skeleton by attachment of amorphous precursor particles, including hydrated and anhydrous amorphous calcium carbonate (ACC- H_2O and ACC).³ Then, this result was reproduced in five other genera and expanded to include both particle attachment and ion attachment to achieve dense, space-filling

skeletons at the nano- and microscales.⁴ Particles were assumed to nucleate and grow inside intracellular vesicles, within the calcicoblastic epithelium—that is, the cell layer that deposits the coral skeleton and tightly envelops the forming surface. These vesicles were presumed to be filled with intracellular calcifying fluid (ICF), with closely biologically controlled chemical composition, favoring particle formation. Once formed, intracellular particles are presumed to be delivered, exocytosed, and attached to the forming surface of

Received: October 28, 2021

Published: January 17, 2022



the coral skeleton.⁴ Between the calciblastic epithelium and the coral skeleton is a small amount, 1–2 μm thick,^{5,6} of liquid or gel termed extracellular calcifying fluid (ECF). The ECF is known to acidify when seawater acidifies,² because the ECF is partly open to seawater.⁷ In contrast, the ICF is intracellular; thus, it is expected to be precisely controlled by cells and not at all open to seawater. (Embryonic corals may differ.⁶)

To simulate OA in aquaria, Venn et al.² bubbled CO_2 in seawater and observed the effects on the coral calcification rate, on pH in the ECF, and in the cytoplasm of calciblastic cells. With four different seawater pH values—8.1, 7.8, 7.4, and 7.2—and three different coral species—*Stylophora pistillata*, *Pocillopora damicornis*, and *Acropora hyacinthus*—they observed that the daytime calcification rate decreased significantly for *Pocillopora* and *Acropora* but remained constant for *Stylophora*. The ICF pH in intracellular vesicles was not measured, but the intracellular pH in the cytoplasm of calciblastic cells decreased slightly and similarly (pH changed by ~ -0.3 for all genera from control values ~ 7.4), as did the ECF pH measured during the day (~ -0.5 for all genera from control values ~ 8.2). The parameter that changed most dramatically and differently across genera was the ECF pH measured at night: ~ -0.4 , ~ -0.6 , and ~ -0.7 change for *Stylophora*, *Pocillopora*, and *Acropora*, respectively. The decrease of calcification and ECF night-time pH with OA for these three corals is shown in Figure 1.

The ECF night-time pH accompanies the observed decrease in night-time calcification rate for the three genera, and best distinguishes them from one another in their resilience to OA. Clearly, for all genera, the ECF night-time pH is biologically controlled, as indicated by the different slopes for the three genera, all of them above the 1:1 line in Figure 1b. Is it possible that intracellular particle formation and ICF are less or not at all affected by OA, but once the particles are exocytosed and exposed to ECF they dissolve as the ECF pH decreases with OA? This would explain the difference across genera observed at night but not during the day.² Biomineralization and respiration proceed day and night, whereas photosynthesis is only active during the day. Thus, it is not surprising that biomineralization conditions differ between day and night. Photosynthesis, done by the coral polyp animal's symbiont dinoflagellates, changes the chemistry internal to the animal in two different ways: it removes aqueous CO_2 and therefore increases the pH in the surrounding fluids. Furthermore, photosynthesis produces carbohydrates that feed the coral polyp animal, thus providing metabolic energy, which the animal can use to better control its internal chemistry, and specifically the ECF day-time pH.

If the nucleation and growth of nanoparticles occurs in intracellular vesicles, as hypothesized previously,⁴ it should be possible to observe particles in intracellular vesicles in the calciblastic cells in all coral genera—those extremely sensitive to OA, such as *Acropora*, and those resilient to OA, such as *Stylophora*. To test this hypothesis, we searched for particles outside the forming skeleton surface and strived to analyze the mineral phases present in such particles, if they exist, in three diverse corals.

Where the particles nucleate and grow before they attach to the forming skeleton surface, in the ECF or in the hypothesized but never directly observed ICF, makes a significant difference. If they nucleate and grow in the ECF, OA will be inescapably fatal for the most sensitive corals, such as *Acropora*.

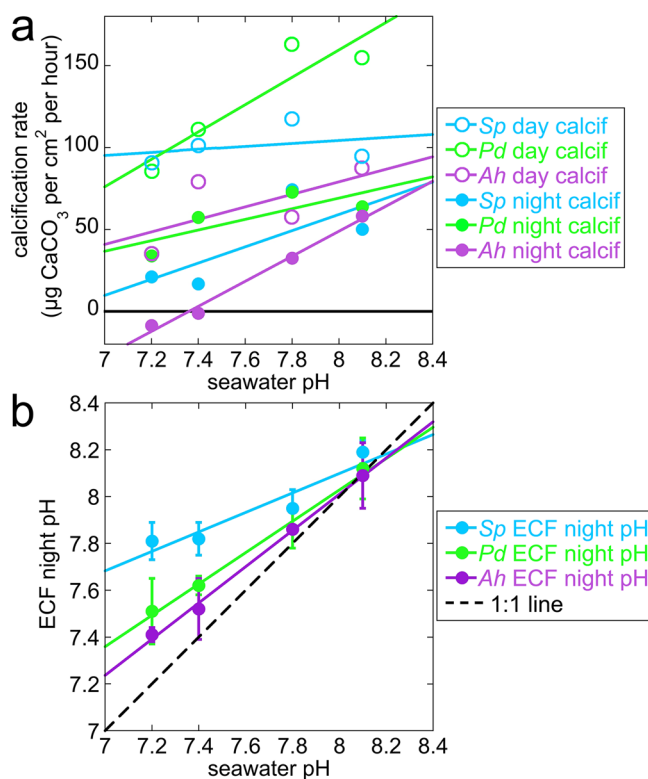


Figure 1. (a) Calcification rate and (b) night-time pH measured in extracellular calcifying fluid (ECF), between calciblastic epithelium and forming skeleton surface, as seawater pH decreases in simulated ocean acidification (OA, pH 8.1 \rightarrow 7.2) experiments in three coral genera and species: *Stylophora pistillata* (*Sp*, light blue), *Pocillopora damicornis* (*Pd*, green), and *Acropora hyacinthus* (*Ah*, purple). These are selected, replotted data from Venn et al., 2019.² (a) During the day (open circles) the calcification rate is constant for *Stylophora*, but it decreases with OA for *Pocillopora* and *Acropora*. At night, calcification decreases with OA for all genera, but especially for *Acropora*, which goes below zero (black solid line); thus, the skeleton formed during the day dissolves at night. (b) The pH values in the ECF during the day, when photosynthesis is active, decrease to 7.8 identically for all three genera; thus, they are omitted here. Only night-time pH values in the ECF are shown, as they vary dramatically across the three genera. The solid lines are linear fits of the data; the 1:1 line (black dashed line) is where $\text{pH}_{\text{ECF}} = \text{pH}_{\text{seawater}}$. Clearly, as the seawater pH decreases, the ECF night-time pH decreases, but at slower rates for all genera compared to seawater. *Stylophora* ECF pH is the slowest, *Pocillopora* intermediate, and *Acropora* the fastest, that is, closest to the seawater pH decrease with OA.

If instead nucleation and growth of particles occurs intracellularly, even the most sensitive genera may have a chance at surviving OA. As long as the pH of the oceans stays above the threshold of net dissolution, the animals will still be able to form new skeletons, even if ECF conditions prevent particle nucleation and growth.

The supersaturation with respect to aragonite is

$$\Omega_{\text{aragonite}} = \frac{[\text{Ca}^{2+}][\text{CO}_3^{2-}]}{K_{\text{sp}}}$$

where the solubility product is $K_{\text{sp}} = 7.184$, as obtained by Sevilgen et al.⁸ using the salinity values in Mucci.⁹ As shown by Cohen and Holcomb,¹⁰ nucleation of aragonite occurs at very high saturation states, $\Omega_{\text{aragonite}} \geq 20$, whereas at lower supersaturation states, with $6 < \Omega_{\text{aragonite}} < 19$, crystal growth

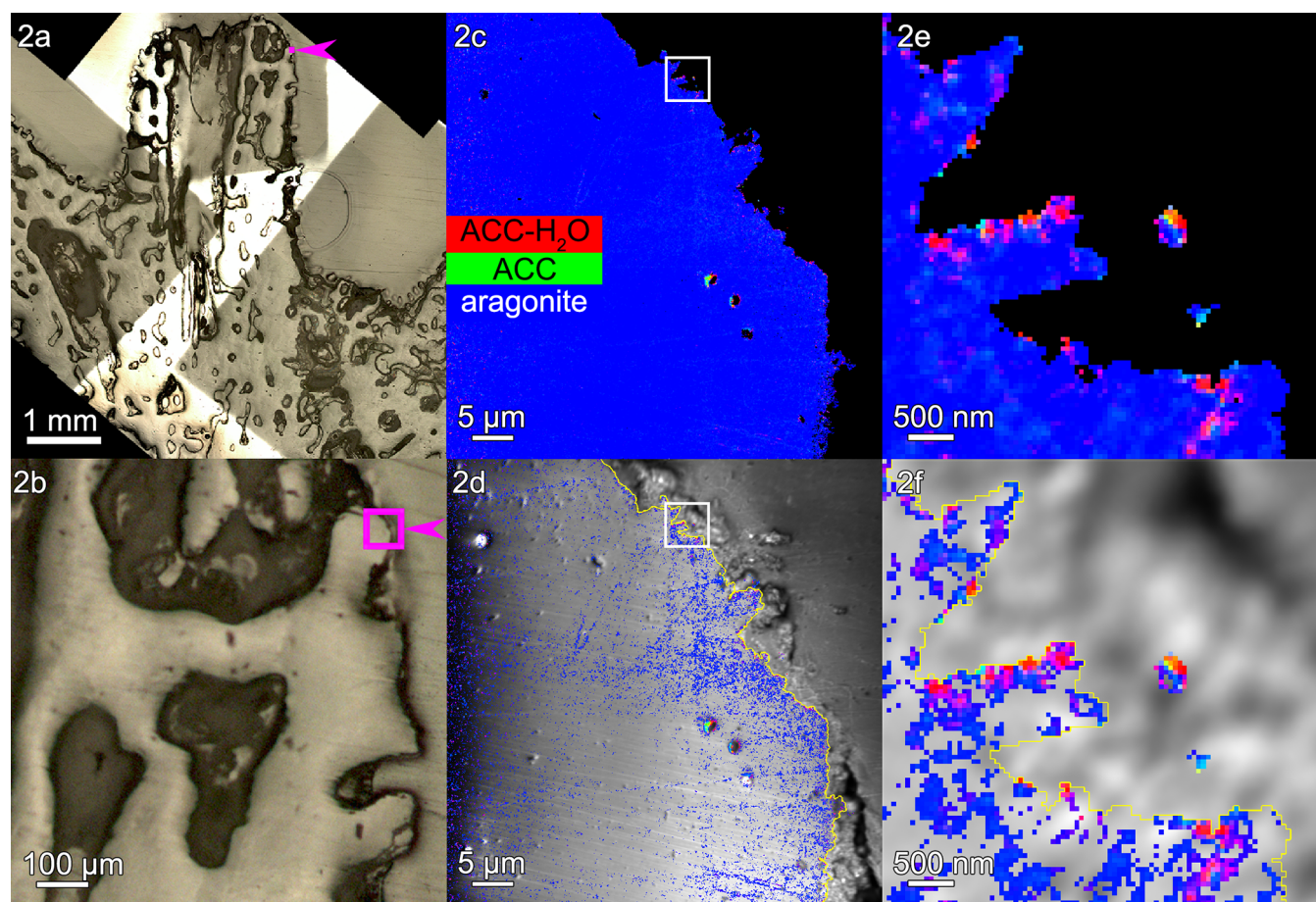


Figure 2. *Acropora* sp.: (a, b) polarized light microscopy (PLM) images and (c) a component map with a black mask where the Ca signal is undetectable and pixels colored according to the mineral phase spectroscopically observed. In this and all other component maps in this work, red pixels are ACC-H₂O, green pixels are ACC, and blue pixels are aragonite. The component spectra used to obtain all component maps are shown in Figure S1. (d) Average PEEM image overlaid with the component map, with both black mask and pure blue aragonite removed. (e, f) One region of interest, boxed in panels c and d, magnified here to show the precise locations of both intra- and extraskeletal amorphous pixels. Extraskeletal particles are no farther than 2 μm outside the skeleton's surface (yellow line in panels d and f), are mostly amorphous, and are assumed to be inside the calcicoblastic epithelium. Intraskelatal amorphous pixels in panel d extend several micrometers inside the yellow line. See Figure S2 for more images of this area.

is favored over nucleation.¹⁰ For other carbonates, amorphous and crystalline, similar supersaturation ranges are expected for nucleation and growth. In the ECF, the supersaturation measured by Sevilgen et al.⁸ in *Stylophora* is $\Omega_{\text{aragonite}} = 12$; thus, only crystal growth occurs, and this must be growth by ion attachment. If nanoparticles are observed in the tissue, they require that ICF conditions be appropriate for nucleation; thus, the supersaturation in ICF must be greater than in ECF, or else nucleation could not occur.¹⁰ Such intracellular vesicles, and the ICF they contain, in which particles nucleate and grow, have been observed in single cells of sea urchin embryos, where they contained ICF with more than 1 M calcium!¹¹

If such high-concentration and supersaturated droplets of solution exist intracellularly in corals, sea urchin embryos,¹¹ or adult regenerating sea urchin spines,¹² they must be confined by vesicles, with phospholipid membranes that keep them well isolated from the cytoplasm. This is because the calcium concentrations necessary for nucleation (mM–M) are toxic for any eukaryotic cells, whose cytoplasm has orders of magnitude lower concentrations (nM).⁴

RESULTS AND DISCUSSION

Extraskeletal Particles. Using photoemission electron microscopy (PEEM), we analyzed species that are representative of three different genera of corals: one extremely sensitive to OA, *Acropora* sp.; one resilient to OA, *S. pistillata*; and one with unknown response to OA, *Turbinaria peltata*. Mapping the spectral components at the surface of the fresh, forming coral skeleton, we observed that all genera form calcium carbonate particles just outside (<2 μm) the skeleton surface, indicated by a yellow line, and just inside the surface (1–2 μm), in the recently deposited skeleton (see Figures 2–4 and Figures S2–S4).

The extraskeletal particles observed vary in size between 200 nm and 1 μm, and spectromicroscopic analysis of their composition reveals a mix of ACC-H₂O, ACC, and aragonite. The density of extraskeletal particles varies from area to area, ranging from ~1 to 30 particles/μm³ in the probed volume, which ranges from ~1 to 7 μm³ for each area, as shown in Table S1. The density of extraskeletal particles was expected to be small, as previously observed and calculated in regenerating sea urchin spines,¹² because the probing depth of PEEM component mapping at the Ca L-edge is only 3 nm, as shown

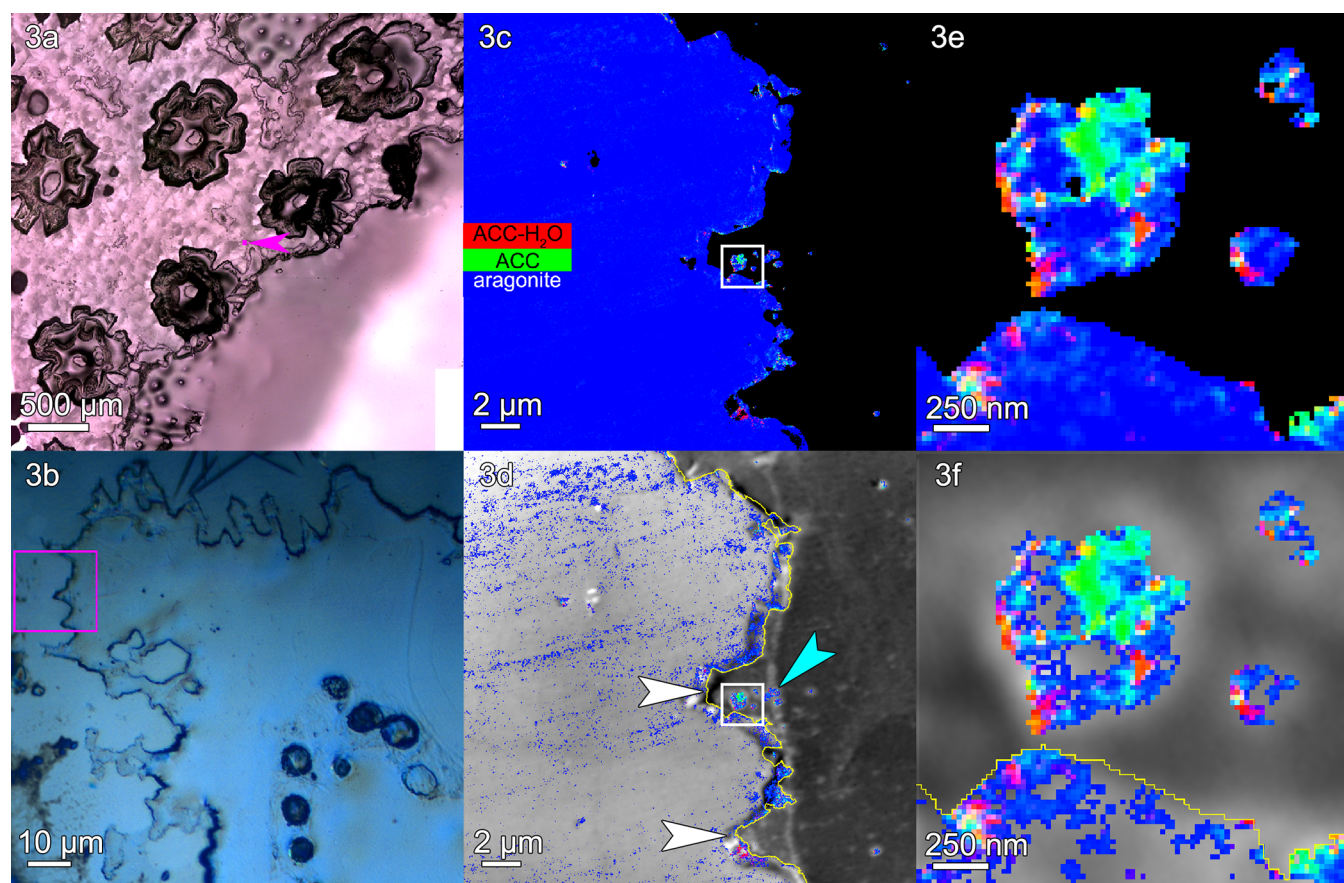


Figure 3. *Stylophora pistillata*: (a) PLM image, (b) DIC image, (c) a component map, and (d) an average PEEM image overlaid with the component map, as described in Figure 2. (e, f) The regions boxed in panels c and d are magnified here to show amorphous particles where calciblastic cells are expected. This region shows several scars left by desmocytes, the cells that bind the calciblastic epithelium to the skeleton and form 3- μm -deep V-shaped scars, indicated by white arrows in panel d. Distinct particles are visible just outside the skeleton surface (e.g., cyan arrowhead in panel d, and three particles in panel f). These extraskelatal particles have both a greater percentage of amorphous pixels and a greater concentration of amorphous phases per pixel, compared to the skeleton surface or bulk (Tables S2 and S3). Extraskelatal particles are mostly amorphous within the calciblastic epithelium, $<2\ \mu\text{m}$ outside the yellow line in panels d and f. Intraskelatal amorphous pixels in panel d extend $\sim 1\ \mu\text{m}$ inside the yellow line. See Figure S3 for more images of this area.

in refs 13 and 14; thus, even higher densities for particles appear sparser in such a thin slice.

The location of extraskelatal calcium carbonate particles is consistent with them being intracellular, inside calciblastic cells. These particles must have formed where they were observed, and when the tissue was fixed they were interrupted in their transfer to the forming skeleton surface, where, in time, they would have crystallized. Several observations, explained below, support this deduction.

First, the grayscale PEEM images at the Ca L-edge in Figures 2–4, panels d, and all other areas in Figure S5 are not good enough to identify cells or cell structures. However, calciblastic cells are well known to envelop the forming skeleton, and all of it,⁵ and are well preserved by the fixation method used here and previously.⁴ Thus, any Ca-rich extraskelatal nanoparticles observed within a $2\ \mu\text{m}$ distance can safely be interpreted as intracellular to calciblastic cells.⁵ The distances outside the skeleton surfaces (yellow lines in panels d and f) in Figures 2–4 and in four additional areas per genus are consistently within $\sim 2\ \mu\text{m}$ (Figure S5). Representative single-pixel spectra for each mineral phase and each coral skeleton in Figures 2–4 are shown in Figure S6.

Second, given the supersaturation of the ECF, $\Omega_{\text{aragonite}} = 12$ measured in *Stylophora*, nucleation of particles in the ECF is extremely unlikely.^{8,10}

Third, amorphous pixels, either ACC- H_2O or ACC, are observed in greater percentage in extraskelatal particles than intraskelally, even when comparing extraskelatal particles with only the skeleton surface, as shown in Tables S2 and S3; thus, intracellular particles are distinct, and not simply material dislodged from the skeleton during embedding or polishing. Figures 2–4, panels e and f, show such extraskelatal and intracellular particles and their amorphous phases just outside the surface of the forming skeleton (yellow line). Intraskelatal amorphous pixels are substantially less spatially dense than in extraskelatal particles; thus, there is a distinct chemical difference between amorphous phases inside or outside the skeleton.

Fourth, if extraskelatal particles were not present intracellularly but were in the ECF, they would have been washed away when the corals were fixed and then rinsed tens of times, so there must have been something holding the particles in place—likely the calciblastic cells, as these are well known to envelop the forming skeleton.⁵ It is possible that more particles were originally present that were washed away during the tens

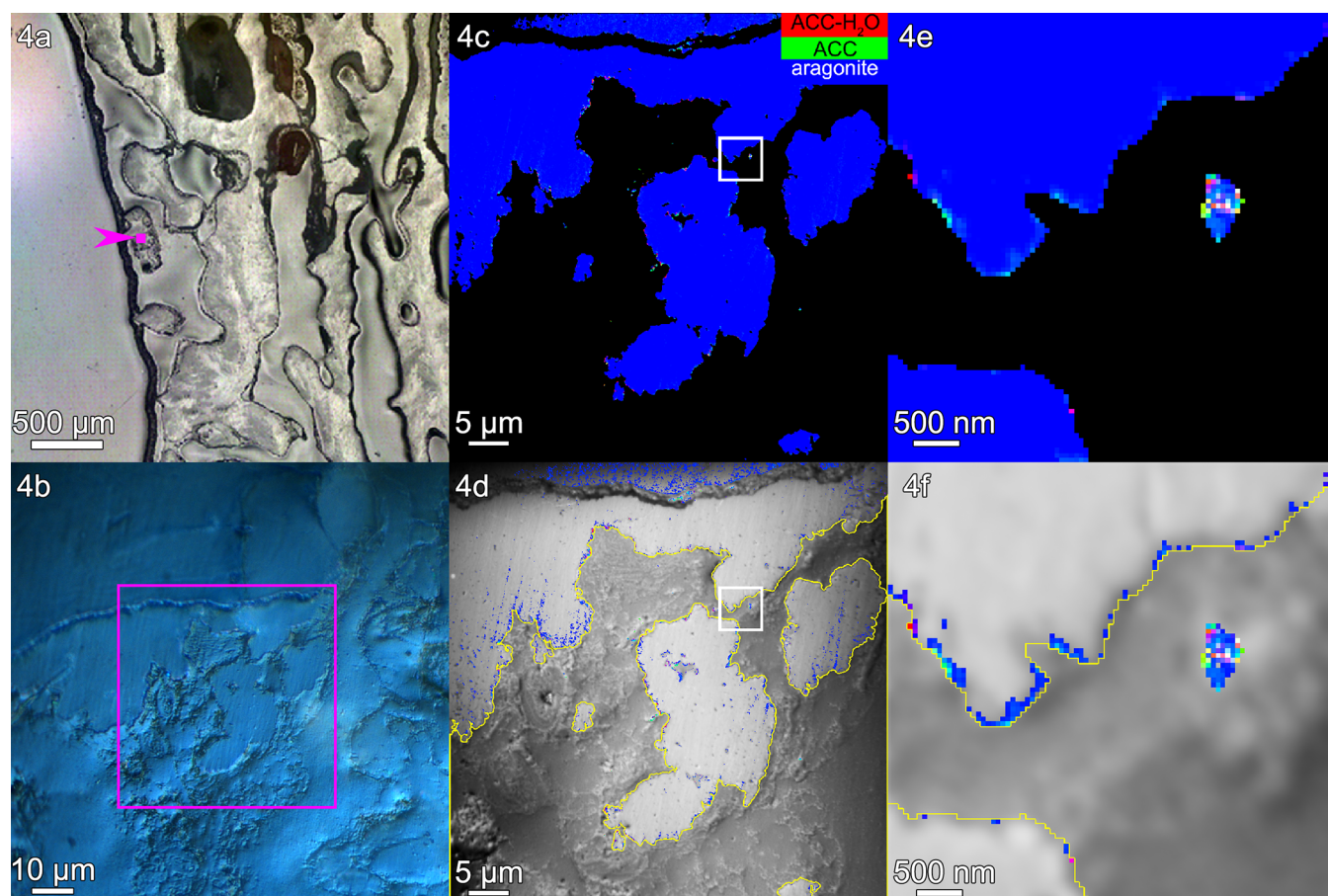


Figure 4. *Turbinaria peltata*: (a) PLM image, (b) Differential Interference Contrast (DIC) image, (c) component map, and (d) average PEEM image overlaid with the component map, as described in Figure 2. (e, f) The regions boxed in panels c and d are magnified here to show amorphous particles where calicoblastic cells are expected. Amorphous pixels also appear along the edge of the skeleton. Extraskelatal particles are mostly amorphous within the calicoblastic epithelium, $<2 \mu\text{m}$ outside the yellow line in panels d and f. Intraskelatal amorphous pixels in panel f extend $<1 \mu\text{m}$ inside the yellow line. See Figure S4 for more images of this area.

of rinsing steps. No conclusions were made based on lost particles.

All extraskelatal particles observed here could also be localized within a network of organic fibrils¹⁵ or filopodia⁶ that were recently observed, using cryo-scanning electron microscopy, between cells and skeleton.⁶ These occur between the skeleton growing surface and calicoblastic cells or desmocytes, alike, and are attached to the skeleton surface;¹⁵ thus, even where cells were detached from the skeleton during sample preparation, fibrils could, in principle, remain attached. Since the fibrils are expected to contain Ca-rich particles, it is possible that some or all the extraskelatal particles observed here in all genera are within fibrils. It is important to note that these fibrils are still part of calicoblastic cells; thus, particles within fibrils should still be considered intracellular. Particles in either cell bodies or fibrils protruding from cell bodies are collectively referred to in this work as in-tissue or intracellular extraskelatal particles.

The Ca-rich biggest particle in Figure 3e,f is comparable in size and position to one of the vacuoles observed by Clode and Marshall in a desmocyte (labeled V in their Figure 1),¹⁵ although this similarity must be further investigated to be confirmed.

Extraskelatal amorphous particles, consistent with intracellular vesicles, were also observed in regenerating sea urchin spines.¹²

Skeletal Surface Crystallization Rates Differ across Genera. The most striking difference across genera is the thickness of the surface layer containing intraskelatal amorphous pixels, measured from the yellow line at the surface of each skeleton. This thickness is $2.1 \mu\text{m}$ in *Acropora*, $1.1 \mu\text{m}$ in *Stylophora*, and $0.9 \mu\text{m}$ in *Turbinaria*. The average measurements of these thicknesses are shown in Figure 5, and all the precise data from 15 areas in three genera are presented in Table S4. The same trends are visible in Figures 2d, 3d, and 4d, where the pure aragonite blue pixels were removed: intraskelatal amorphous pixels are farther from the surface in *Acropora*, intermediate in *Stylophora*, and closer in *Turbinaria*. Thus, crystallization rates differ across the three genera, as shown in Figure 5.

There are also differences in the composition of these intraskelatal surface bands: *Acropora* has the greatest density of amorphous pixels, and its pixels are mostly ACC-H₂O; *Stylophora* has intermediate amorphous density and mostly ACC pixels; and finally *Turbinaria* has the lowest density and fewest of both ACC-H₂O and ACC pixels (Table S2).

In all genera, almost all pixels observed farther into the skeleton than $1\text{--}2 \mu\text{m}$ were pure aragonite. (In Figure 3d, some lines of pixels were not selected by the Magic Wand because they were non-pure aragonite—these are topographic artifacts caused by scratches on the sample's imperfectly polished surface.)

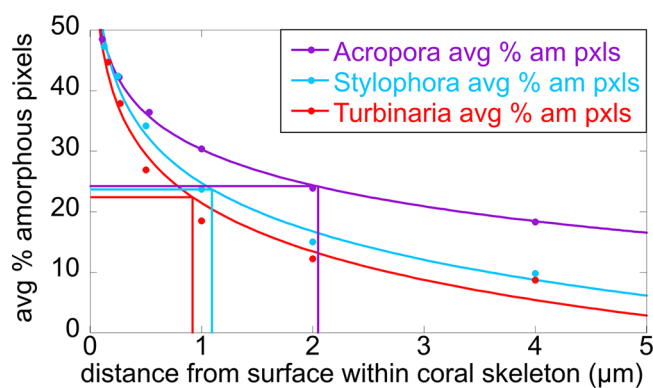


Figure 5. Amorphous, soluble thickness decays with distance from the skeleton surface. Comparison of the three genera analyzed here, for percentage of amorphous pixels (either ACC-H₂O or ACC) as a function of distance from the surface, indicated by a yellow line in Figures 2–4. Each percentage is averaged over the five areas analyzed per genus (Table S4), the averages are displayed as circles, and the solid lines are logarithmic decays (among others tested, a logarithmic decay provided better fits, with $R > 0.98$). The half-lengths (vertical lines) are the distances at which the amorphous pixels have decayed to 50% of the surface value for that genus (horizontal lines). The half-lengths are 2.1 μm for *Acropora*, 1.1 μm for *Stylophora*, and 0.9 μm for *Turbinaria*.

The density of amorphous pixels was quantified in each genus by measuring the percentage of amorphous pixels within 2 μm of the skeleton surface. For *Acropora*, *Stylophora*, and *Turbinaria*, we found that approximately 24%, 15%, and 12% of the pixels contained amorphous phases. These values were obtained from 15 areas analyzed. The precise values from each area and genus are shown in Table S2. The areas in Figures 2–4 have slightly different percentages of amorphous pixels than the average, but they follow the same trend as the average, with *Acropora* having the most amorphous and *Turbinaria* the most crystalline 2- μm -thick surface layer (Table S2).

We note that the times for sample preparation and analysis varied between 15 and 45 h post-mortem. All of these times are immensely longer than the crystallization rate of ACC-H₂O in laboratory conditions, which takes less than 1 min, especially in contact with water.¹⁶ Therefore, the observed amorphous phases are biologically stabilized, or they would not be observable in these experiments. Amorphous-phase stabilizing molecules are well known to exist in biominerals.^{17–23}

The increased amorphous content observed in the surface layer of *Acropora* skeleton means that these amorphous phases last longer during the process of skeleton formation in *Acropora*. Thus, crystallization of amorphous phases is slow in *Acropora*, faster in *Stylophora*, and fastest in *Turbinaria*.

This observation directly explains why different genera vary in sensitivity to OA, as shown in Figure 1. The forming surface in *Acropora* skeletons crystallizes slowly from its amorphous precursors; thus, newly attached ACC-H₂O and ACC particles are exposed to the ECF for a longer time.

ACC and ACC-H₂O are well known to be more soluble than crystalline aragonite in water;²⁴ thus, they can dissolve in ECF, as occurs for *Acropora* at night (Figure 1). The solubility product $K_{\text{sp,ACC}}$ is $\sim 100\times$ larger than $K_{\text{sp,arag}}$ in deionized water,²⁴ making ACC significantly more soluble than aragonite. The solubility of ACC in ECF or even in seawater conditions is not known, but it is certainly greater than that of aragonite in those conditions as well. In contrast, the faster-crystallizing

skeleton surface in *Stylophora* exposes more insoluble aragonite than soluble ACC to night-time ECF, thus reducing dissolution. While this may not be the only factor contributing to OA resilience, these data suggest that *Turbinaria* should be even more resilient to OA than *Stylophora*, due to its fastest crystallization rate observed here. We stress that this is the crystallization rate from the amorphous precursors to crystalline aragonite, not the calcification rate, which is known to be slower in *Turbinaria* than in *Stylophora*.^{25,26} There are at present no data on *Turbinaria*'s resilience to OA.

Notice that the calcification rate in *Acropora* is lower than in *Stylophora*, which is in turn lower than in *Pocillopora*, as shown in Figure 1, for both day- and night-time calcification. The synthesis rate of precursors is equal to the calcification rate, independent of crystallization rate. Thus, the thickest amorphous layer observed in *Acropora* cannot be caused by greater production of amorphous precursor, because *Acropora* is the slowest calcifier. We also observe a lower density of extraskeletal particles in *Acropora* than in both *Turbinaria* and *Stylophora* (Table S1), consistent with the lower calcification rate (Figure 1).

The origin of differing crystallization rates is not explored in this study. We speculate that either organic molecules or elemental impurities stabilize amorphous phases for a longer time in *Acropora*. For instance, magnesium is known to stabilize ACC in sea urchin spines,^{16,27} and proteins are known to do the same in sea urchin spicules.¹⁷

CONCLUSION

Here, analyzing fresh corals inside and outside the surface of the forming skeletons, we observed particles consistent with intracellular localization, presumably inside calciblastic cells.

Intraskeletal amorphous phases localized near the skeleton's surface contain, respectively, a lower or greater percentage of the amorphous phases compared to the extraskeletal particles or the skeleton bulk, which is almost completely crystalline aragonite. These spectroscopically detectable localizations in space and phase transition trends are consistent with previous models of coral skeleton biomineralization.^{4,28,29} They are also consistent with a time sequence in which extraskeletal amorphous nanoparticle nucleation and growth in intracellular vesicles is followed by attachment to the growing surface of the skeleton,^{30,31} followed by gradual crystallization of the amorphous phases into crystalline aragonite.

The precise chemical environment (ICF) and cellular location in which the particles nucleate remain unknown. We observe directly extraskeletal particles, likely in intracellular vesicles within calciblastic cells forming the epithelium that envelops the growing skeleton surface.

Once the particles are exocytosed into the ECF and attach to the growing skeleton surface, they are exposed to increasingly lower pH during OA. The partial control of ECF pH will slow down but not completely counter the effect of OA on the ECF, which is partly open to seawater,⁷ especially for sensitive corals such as *Acropora*, where with seawater pH 7.2, the ECF night-time pH is as low as 7.4, as shown in Figure 1.

The differential sensitivity of calcification to OA, shown in Figure 1A, is elegantly explained by faster or slower crystallization of the forming skeleton surface, which makes it less or more soluble, and thus more or less resilient to OA. We observed less-amorphous surfaces in resilient *Stylophora* than in vulnerable *Acropora*, and even less in *Turbinaria*, whose

response to OA is unknown but is predicted, on the basis of these data, to be even more resilient than *Stylophora*.

METHODS

Samples. All corals were obtained live from Albany Aquarium, Albany, CA, USA. First, 1-cm fragments of skeleton and tissue were fixed to preserve the tissue and all its nanoparticle content, and then they were dehydrated with increasing concentrations of ethanol as described by Sun et al. in 2020.⁴ The *Stylophora* and *Turbinaria* samples were then embedded into EpoFix (EMS, Hatfield, PA, USA), the *Acropora* sample was embedded in Solarez (Solarez, Vista, CA, USA) and UV-cured, and all three were polished, coated with 1 nm Pt in the regions to be analyzed, and 40 nm Pt elsewhere, as described in refs 32–35.

The three coral samples were analyzed with component mapping approximately 1–2 days after they were fixed. Precisely, the analysis lasted 13–24 h post-mortem for *Acropora* (14.5–15 for the data in Figure 2), 23–44.5 h post-mortem for *Stylophora* (44–44.5 for the data in Figure 3), and 24.5–36 h post-mortem for *Turbinaria* (25.5–26 for the data in Figure 4).

The post-mortem times of the corals differ, but this does not invalidate the deduced amorphous precursor crystallization rates. The rate of crystallization for ACC in the lab is on the order of seconds;¹⁶ thus, the post-mortem times used here are many orders of magnitude larger, making differences between them insignificant. Furthermore, the longest post-mortem sample, *Stylophora*, does not contain the fewest amorphous pixels, implying that these phases are stabilized biologically^{17–23} and last days post-mortem. Finally, all sample preparations greatly reduce the exposure of the amorphous phases to water and air, both of which induce ACC crystallization.³⁶

Component Mapping. PEEM images, component maps, and spectra shown in all figures were acquired using the photoemission electron microscope (PEEM) at the Advanced Light Source on beamline 11.0.1.1. All data were acquired across the Ca L-edge. The intracellular particles observed in calcicoblastic cells vary in size between 200 nm and 1 μm , and spectromicroscopic analysis of their composition reveals a mix of hydrated and anhydrous amorphous calcium carbonate (ACC-H₂O and ACC) and aragonite.

PEEM images were taken with 54, 24, or 56 nm pixel resolution for Figures 2, 3 or 4, respectively, and 3 nm probing depth.¹³ Each stack of 121 PEEM images contained 10⁶ pixels/image, and thus 10⁶ complete Ca spectra. All Ca stacks of images were acquired between 340 and 360 eV, with 0.1 eV energy steps between 345 and 355 eV where the Ca peaks are, and 0.5 eV steps outside of this range. All Ca spectra were acquired with circular polarization to minimize crystal orientation effects.

Images were stacked to produce component maps, in which each pixel spectrum is best-fitted to a linear combination of known “component spectra”, using IGOR Pro Carbon 8 with open-source GG Macros, available free of charge from ref 37. The “Cni7” component spectra (Figure S1) are provided as Supporting Information.

Figures 2d, 3d, and 4d were all made by overlaying the component map from Figures 2c, 3c, and 4c on a PEEM average image in Adobe Photoshop and then using the Magic Wand tool to remove both black (the Ca poor mask) and pure blue (aragonite) from the component map, with a threshold of 26, which is 10% of 255.

The component maps in Figures 2–4 are “brightness enhanced”³⁷ to improve visibility of amorphous phases. Before brightness enhancement, the amounts of RGB add up to 255 and are entirely quantitative. Brightness enhancement is accomplished by making the color value of the largest percentage component 255 and then scaling up the other two components proportionally. For example, if a pixel has RGB amounts [25,25,205], thus, approximately 10% ACC-H₂O, 10% ACC, and 80% aragonite, brightness enhancement changes its RGB values to [31,31,255]. All operations using the Magic Wand tool in Adobe Photoshop were performed on non-brightness-enhanced pMaps of the component of interest.³⁷ In Figures 2–4, the epoxy black pixels and aragonite blue pixels deleted from panels d and f were

selected using the Magic Wand on non-brightness-enhanced RGB maps, so they were quantitatively accurate.

The black masks in Figures 2c, 3c, and 4c that cover the irrelevant parts of component maps are all produced from a combination of three different masks termed “difference mask”, “ χ^2 mask”, and “manual mask”. The difference mask covers all pixels with a zero or near-zero Ca concentration. It is produced in the GG Macros³⁷ by digital subtraction of two images, acquired above and below the Ca L-edge at 352.6 and 344 eV energies, respectively. More precisely, in order to eliminate noise, each image used in the subtraction is the average of multiple images (five on-peak, nine off-peak), acquired at and around the stated energies. The resulting Ca concentration map is shown in Figure S7. The Ca concentration map is then thresholded so all pixels in the image with zero or near-zero Ca concentration are masked off and displayed as black. The threshold value is determined accurately by zooming in on a skeleton edge region and adjusted numerically until all the spectra at the skeleton edge with acceptable signal/noise ratio and distinct and identifiable Ca spectral peaks are retained, and the others are discarded. This numeric adjustment of the threshold is repeated in several regions of skeleton edge to ensure that the difference mask is consistently retaining good- and discarding bad-spectra pixels. The χ^2 mask is produced by first mapping all χ^2 values obtained from the best fit during component analysis of each pixel. Then, a threshold is applied to exclude all χ^2 values above a numeric value, typically $\chi^2 = 0.01$. The resulting χ^2 mask, therefore, makes black all pixels where, for any reason, the fit was poor. Both masks, difference and χ^2 , are then layered on top of one another in Adobe Photoshop. The third “manual mask” is produced by hand to discard (display in black) any spurious single pixels that were not eliminated by the other two masks. The rare single pixels observed are unrealistic, noisy spectra and are clearly Ca-poor in the epoxy or tissue regions. Figure S7 shows PEEM single and average images, the Ca map, and the final black mask over the component map and over the Ca map.

The yellow line, indicating the skeleton surface, was obtained by outlining the black mask (resulting from overlapping difference, χ^2 , and manual masks) from each component map, ignoring particles outside the skeleton and anything masked inside the skeleton. This was achieved by selecting the mask and outlining it with a yellow line using the “Stroke” layer tool in Adobe Photoshop. This line was obtained with 1-pixel resolution (24 nm in *Stylophora*; 54 and 56 nm in *Acropora* and *Turbinaria*) and used throughout all distance and thickness measurements with 1-pixel resolution, leaving no ambiguity about what is inside and outside the skeleton. For visibility and display purposes only, in panels d and f, the yellow line was made 3-pixels wide, expanding outside the skeleton, not to overlap any parts of it. Figure S7 shows the yellow outline and the amorphous pixels overlaid on an average image, as done in Figures 2–4.

We stress that the colored pixels from component maps (panels c and e in all figures) and the grayscale average PEEM image (panels d and f) were obtained from precisely the same Ca stack, not repeated acquisitions. Thus, we made no assumptions on where the Ca signal was high or low, where the tissue was, or where the skeleton was in space. The yellow line position is based exclusively on where the Ca signal is as high as in the mature skeleton. This is a conservative choice that excludes many amorphous pixels, but it is a rigorous one.

Amorphous Pixel Counting. Quantitative measurements of how amorphous the different skeletons surfaces are were performed in Adobe Photoshop and are presented in Tables S2 and S4. To obtain the amorphous pixels vs depth data in Table S4 and Figure 5, first we used the black mask in each area, and then the “Expand” selection tool to include the outermost 4, 2, 1, 0.5, 0.25, and 0.125 μm of skeleton. Next, the black mask was removed from the selection area, and finally the selected band was placed over the ACC-H₂O or ACC proportion maps, that is, the grayscale images that show the proportion, between 0 and 1 or between 0 and 255, of ACC-H₂O or ACC phase in each pixel. Then, using the Magic Wand tool, we selected a pixel that contained 100% of a given phase and varied the tolerance of the wand. To select pixels with at least 10% amorphous phase, a tolerance of 230 was used, which is 90% of 255. Once selected, the number of pixels was measured in “Windows” and “Histogram” in Adobe Photoshop.

For aragonite we used a threshold of 26, which is 10% of 255. All pixel counts from all areas were logged in Microsoft Excel, as presented in Table S4, at the depth specified. Figure 5 was obtained in Kaleidagraph 5.0 for Mac (Synergy Software), where the data were fitted by a logarithmic decay with excellent correlation coefficients: $R = 0.999$ for *Acropora*, $R = 0.995$ for *Stylophora*, and $R = 0.984$ for *Turbinaria*. Other decay functions were tested, including exponential and parabolic, but the correlation coefficients R were lower than for logarithmic decay; hence, the latter was used for Figure 5.

Parallel Component Mapping by the Cnidarians. The Cni7 component spectra used for component mapping were optimized to eliminate any spectral background contributions that are mistakenly interpreted as different phases during component mapping. This undesirable effect was recently discovered for this work, when we processed many stacks of images in parallel, with a group of talented undergraduate students we call “the Cnidarians”, 13 of whom are co-authors of this work. Since October of 2020, the Cnidarians have been processing component mapping spectromicroscopy of biominerals data, collected over the past 10 years. The results of this meta-analysis, done in parallel on the same data by different people, are then compared during biweekly meetings, thus optimizing every choice. There are 5–10 different human choices to make to process component maps, and different people make these choices differently; thus, direct comparison of the results benefits from a diversity of people and greatly improves the final data quality. One major problem was revealed by these comparisons: the energy range used for component analysis (between 345 and 355 eV) greatly affected the outcome of component maps. When using previous component spectra, such as 0608 in Gong et al.,¹⁷ 0709 in DeVol et al.,³⁸ 0823 in Mass et al.,³ or CY1 in Sun et al.,⁴ uneven backgrounds of spectra at the edges of the energy range (around 345 eV or around 355 eV) led to phase assignment differences in component maps when the energy range selected for peak-fitting differed from person to person. This undesirable mistake was eliminated by improving the component spectra so they have identical spectral backgrounds (2 arctan, 1 polynomial), as shown in Figure S1. Using the new “Cni7” component spectra makes the final component map only dependent on real, spectroscopic differences occurring at Ca peaks’ energy positions, not away from Ca peaks, e.g., at 345 or 355 eV. Table S5 shows all the fit parameters for all component spectra.

All data presented in this manuscript have been analyzed by at least 5–10 people, multiple times each, using different component spectra. Once we converged on using the Cni7 component spectra, 5 people analyzed these data in parallel, making individual choices on multiple parameters, e.g., threshold for difference mask and χ^2 mask, peak shift in energy acceptable interval, etc. The data presented are the best fits to the data, because, even after small changes in parameters, the results consistently provide the same locations for amorphous phases in the skeleton and extraskeletal particles. The precise percentage of each phase fluctuates slightly, by $\sim 10\%$.

The component spectra, “Cni7”, were generated by P.U.P.A.G. using spectra taken from several biominerals (Figure S1). Component spectra for ACC-H₂O and ACC were generated from averaged spectra taken from single pixels in sea urchin spines which previous analysis showed to be at least 90% of the desired component. The same process was applied to coral skeletons for the aragonite component spectra. For each component, more than 1000 single-pixel spectra were aligned in energy and averaged, and then we subtracted the backgrounds using a pre-edge linear fit for each spectrum. We then peak-fitted each spectrum, using the background (third-order polynomial and two arctangents) obtained for aragonite for all spectra identically.

■ ASSOCIATED CONTENT

SI Supporting Information

The Supporting Information is available free of charge at <https://pubs.acs.org/doi/10.1021/jacs.1c11434>.

Figures S1–S7, showing component spectra Cni7, polarized light micrographs, component maps of all 15

areas analyzed in this work, single-pixel spectra, single PEEM image, average image, and a Ca concentration map; Tables S1–S5, showing extraskeletal particle density, intra- and extra-skeletal percentage of amorphous pixels, percentage of amorphous pixels vs distance from surface within the skeletons, and component spectra peak-fitting parameters (PDF)

Cni7 files: component spectra for ACC-H₂O, ACC, and aragonite (ZIP)

■ AUTHOR INFORMATION

Corresponding Author

Pupa U. P. A. Gilbert – Department of Physics and Departments of Chemistry, Materials Science and Engineering, and Geoscience, University of Wisconsin, Madison, Wisconsin 53706, United States; Chemical Sciences Division, Lawrence Berkeley National Laboratory, Berkeley, California 94720, United States; orcid.org/0000-0002-0139-2099; Email: pupa@physics.wisc.edu

Authors

Connor A. Schmidt – Department of Physics, University of Wisconsin, Madison, Wisconsin 53706, United States
Cayla A. Stifler – Department of Physics, University of Wisconsin, Madison, Wisconsin 53706, United States
Emily L. Luffey – Department of Physics, University of Wisconsin, Madison, Wisconsin 53706, United States
Benjamin I. Fordyce – Department of Physics, University of Wisconsin, Madison, Wisconsin 53706, United States
Asiya Ahmed – Department of Physics, University of Wisconsin, Madison, Wisconsin 53706, United States
Gabriela Barreiro Pujol – Department of Physics, University of Wisconsin, Madison, Wisconsin 53706, United States
Carolyn P. Breit – Department of Physics, University of Wisconsin, Madison, Wisconsin 53706, United States
Sydney S. Davison – Department of Physics, University of Wisconsin, Madison, Wisconsin 53706, United States
Connor N. Klaus – Department of Physics, University of Wisconsin, Madison, Wisconsin 53706, United States
Isaac J. Koehler – Department of Physics, University of Wisconsin, Madison, Wisconsin 53706, United States
Isabelle M. LeCloux – Department of Physics, University of Wisconsin, Madison, Wisconsin 53706, United States
Celeo Matute Diaz – Department of Physics, University of Wisconsin, Madison, Wisconsin 53706, United States
Catherine M. Nguyen – Department of Physics, University of Wisconsin, Madison, Wisconsin 53706, United States
Virginia Quach – Department of Physics, University of Wisconsin, Madison, Wisconsin 53706, United States
Jaden S. Sengkhamee – Department of Physics, University of Wisconsin, Madison, Wisconsin 53706, United States
Evan J. Walch – Department of Physics, University of Wisconsin, Madison, Wisconsin 53706, United States
Max M. Xiong – Department of Physics, University of Wisconsin, Madison, Wisconsin 53706, United States
Eric Tambutté – Department of Marine Biology, Centre Scientifique de Monaco, 98000 Monaco, Principality of Monaco
Sylvie Tambutté – Department of Marine Biology, Centre Scientifique de Monaco, 98000 Monaco, Principality of Monaco
Tali Mass – Marine Biology Department, University of Haifa, Mt. Carmel, Haifa 31905, Israel

Complete contact information is available at:
<https://pubs.acs.org/10.1021/jacs.1c11434>

Funding

P.U.P.A.G. received 40% support from DOE–BES–Chemical Sciences, Geosciences, Biosciences–Geosciences Grant DE-FG02-07ER15899, 40% support from the Laboratory Directed Research and Development (LDRD) program at Berkeley Lab, through DOE–BES, under Award Number DE-AC02-05CH11231, and 20% support from NSF Biomaterials Grant DMR-1603192. All PEEM experiments were done at the Advanced Light Source (ALS), which is supported by the Director, Office of Science, Office of Basic Energy Sciences, U.S. Department of Energy under Contract No. DE-AC02-05CH11231. T.M. received funding from the European Research Council under the European Union's Horizon 2020 research and innovation program (grant agreement no. 755876).

Notes

The authors declare no competing financial interest.
Pupa U. P. A. Gilbert was previously publishing as Gelsomina De Stasio.

ACKNOWLEDGMENTS

We thank Jun “Jay” Zhang for preparing the *Acropora* sample, and Andreas Scholl, Rajesh V. Chopdekar, and Chang-Yu Sun for technical help during beamtime.

ABBREVIATIONS

ACC, amorphous calcium carbonate anhydrous; ACC-H₂O, amorphous calcium carbonate hydrated; OA, ocean acidification; ECF, extracellular calcifying fluid; ICF, intracellular calcifying fluid; PEEM, photoemission electron microscopy; RGB, red, green, and blue

REFERENCES

- (1) Eyre, B. D.; Cyronak, T.; Drupp, P.; De Carlo, E. H.; Sachs, J. P.; Andersson, A. J. Coral reefs will transition to net dissolving before end of century. *Science* **2018**, *359* (6378), 908–911.
- (2) Venn, A.; Tambutté, E.; Caminiti-Segonds, N.; Techer, N.; Allemand, D.; Tambutté, S. Effects of light and darkness on pH regulation in three coral species exposed to seawater acidification. *Sci. Rep.* **2019**, *9* (1), 2201.
- (3) Mass, T.; Giuffrè, A. J.; Sun, C.-Y.; Stiffler, C. A.; Frazier, M. J.; Neder, M.; Tamura, N.; Stan, C. V.; Marcus, M. A.; Gilbert, P. U. P. A. Amorphous calcium carbonate particles form coral skeletons. *Proc. Natl. Acad. Sci.* **2017**, *114* (37), E7670–E7678.
- (4) Sun, C.-Y.; Stiffler, C. A.; Chopdekar, R. V.; Schmidt, C. A.; Parida, G.; Schoeppler, V.; Fordyce, B. I.; Brau, J. H.; Mass, T.; Tambutté, S.; Gilbert, P. U. P. A. From particle attachment to space-filling coral skeletons. *Proc. Natl. Acad. Sci.* **2020**, *117* (48), 30159–30170.
- (5) Tambutté, E.; Allemand, D.; Zoccola, D.; Meibom, A.; Lotto, S.; Caminiti, N.; Tambutté, S. Observations of the tissue-skeleton interface in the scleractinian coral *Stylophora pistillata*. *Coral Reefs* **2007**, *26* (3), 517–529.
- (6) Mor Khalifa, G.; Levy, S.; Mass, T. The calcifying interface in a stony coral primary polyp: An interplay between seawater and an extracellular calcifying space. *J. Struct. Biol.* **2021**, *213*, 107803.
- (7) Venn, A. A.; Bernardet, C.; Chabenat, A.; Tambutte, E.; Tambutte, S. Paracellular transport to the coral calcifying medium: effects of environmental parameters. *J. Exp. Biol.* **2020**, *223* (17), 227074.
- (8) Sevilgen, D. S.; Venn, A. A.; Hu, M. Y.; Tambutté, E.; de Beer, D.; Planas-Bielsa, V.; Tambutté, S. Full in vivo characterization of carbonate chemistry at the site of calcification in corals. *Sci. Adv.* **2019**, *5* (1), eaau7447.
- (9) Mucci, A. The solubility of calcite and aragonite in seawater at various salinities, temperatures, and one atmosphere total pressure. *Am. J. Sci.* **1983**, *283* (7), 780–799.
- (10) Cohen, A. L.; Holcomb, M. Why corals care about ocean acidification: uncovering the mechanism. *Oceanography* **2009**, *22* (4), 118–127.
- (11) Kahil, K.; Varsano, N.; Sorrentino, A.; Pereiro, E.; Rez, P.; Weiner, S.; Addadi, L. Cellular pathways of calcium transport and concentration toward mineral formation in sea urchin larvae. *Proc. Natl. Acad. Sci. U. S. A.* **2020**, *117* (49), 30957–30965.
- (12) Stiffler, C. A.; Killian, C. E.; Gilbert, P. U. P. A. Evidence for a liquid precursor to biomineral formation. *Cryst. Growth Des.* **2021**, *21* (12), 6635–6641.
- (13) Frazer, B. H.; Gilbert, B.; Sonderegger, B. R.; De Stasio, G. The probing depth of total electron yield in the sub keV range: TEY-XAS and X-PEEM. *Surf. Sci.* **2003**, *537*, 161–167.
- (14) Gilbert, P. U. P. A. Photoemission spectromicroscopy for the biomineralogist. In *Biomineralization Sourcebook, Characterization of Biominerals and Biomimetic Materials*; DiMasi, E., Gower, L. B., Eds.; CRC Press: Boca Raton, FL, 2014; pp 135–151.
- (15) Clode, P. L.; Marshall, A. Calcium associated with a fibrillar organic matrix in the scleractinian coral *Galaxea fascicularis*. *Protoplasma* **2003**, *220* (3), 153–161.
- (16) Radha, A. V.; Forbes, T. Z.; Killian, C. E.; Gilbert, P. U. P. A.; Navrotsky, A. Transformation and crystallization energetics of synthetic and biogenic amorphous calcium carbonate. *Proc. Natl. Acad. Sci.* **2010**, *107*, 16438–16443.
- (17) Gong, Y. U.; Killian, C. E.; Olson, I. C.; Appathurai, N. P.; Amasino, A. L.; Martin, M. C.; Holt, L. J.; Wilt, F. H.; Gilbert, P. U. P. A. Phase transitions in biogenic amorphous calcium carbonate. *Proc. Natl. Acad. Sci.* **2012**, *109* (16), 6088–6093.
- (18) Akiva-Tal, A.; Kababya, S.; Balazs, Y. S.; Glazer, L.; Berman, A.; Sagi, A.; Schmidt, A. In situ molecular NMR picture of bioavailable calcium stabilized as amorphous CaCO₃ biomineral in crayfish gastroliths. *Proc. Natl. Acad. Sci.* **2011**, *108* (36), 14763–14768.
- (19) Al-Sawalmih, A.; Li, C.; Siegel, S.; Fratzl, P.; Paris, O. On the stability of amorphous minerals in lobster cuticle. *Adv. Mater.* **2009**, *21* (40), 4011–4015.
- (20) Stephens, C. J.; Ladden, S. F.; Meldrum, F. C.; Christenson, H. K. Amorphous calcium carbonate is stabilized in confinement. *Adv. Funct. Mater.* **2010**, *20* (13), 2108–2115.
- (21) Gal, A.; Habraken, W.; Gur, D.; Fratzl, P.; Weiner, S.; Addadi, L. Calcite crystal growth by a solid-state transformation of stabilized amorphous calcium carbonate nanospheres in a hydrogel. *Angew. Chem. Int.* **2013**, *52* (18), 4867–4870.
- (22) Shaked, H.; Polishchuk, I.; Nagel, A.; Bekenstein, Y.; Pokroy, B. Long-term Stabilized Amorphous Calcium Carbonate—an Ink for Bio-inspired 3D Printing. *Mater. Today Bio* **2021**, *11*, 100120.
- (23) Bentov, S.; Weil, S.; Glazer, L.; Sagi, A.; Berman, A. Stabilization of amorphous calcium carbonate by phosphate rich organic matrix proteins and by single phosphoamino acids. *J. Struct. Biol.* **2010**, *171* (2), 207–215.
- (24) Brečević, L.; Nielsen, A. E. Solubility of amorphous calcium carbonate. *J. Cryst. Growth* **1989**, *98* (3), 504–510.
- (25) Ross, C. L.; DeCarlo, T. M.; McCulloch, M. T. Environmental and physiochemical controls on coral calcification along a latitudinal temperature gradient in Western Australia. *Glob. Change Biol.* **2019**, *25* (2), 431–447.
- (26) Ross, C. L.; Schoepf, V.; DeCarlo, T. M.; McCulloch, M. T. Mechanisms and seasonal drivers of calcification in the temperate coral *Turbinaria reniformis* at its latitudinal limits. *Proc. R. Soc. B: Biol. Sci.* **2018**, *285* (1879), 20180215.
- (27) Rodriguez-Blanco, J.; Shaw, S.; Bots, P.; Roncal-Herrero, T.; Benning, L. G. The role of pH and Mg on the stability and crystallization of amorphous calcium carbonate. *J. Alloys Compd.* **2012**, *536*, S477–S479.

(28) Gránásy, L.; Rátkai, L.; Tóth, G. I.; Gilbert, P. U. P. A.; Zlotnikov, I.; Pusztai, T. Phase-Field Modeling of Biomineralization in Mollusks and Corals: Microstructure vs Formation Mechanism. *JACS Au* **2021**, *1* (7), 1014–1033.

(29) Sun, C.-Y.; Gránásy, L.; Stifler, C. A.; Zaquin, T.; Chopdekar, R. V.; Tamura, N.; Weaver, J. C.; Zhang, J. A. Y.; Goffredo, S.; Falini, G.; Marcus, M. A.; Pusztai, T.; Schoeppler, V.; Mass, T.; Gilbert, P. U. P. A. Crystal nucleation and growth of spherulites demonstrated by coral skeletons and phase-field simulations. *Acta Biomater.* **2021**, *120*, 277–292.

(30) Gilbert, P. U. P. A.; Porter, S. M.; Sun, C.-Y.; Xiao, S.; Gibson, B. M.; Shenkar, N.; Knoll, A. H. Biomineralization by particle attachment in early animals. *Proc. Natl. Acad. Sci.* **2019**, *116*, 17659–17665.

(31) De Yoreo, J. J.; Gilbert, P. U. P. A.; Sommerdijk, N. A. J. M.; Penn, R. L.; Whitelam, S.; Joester, D.; Zhang, H.; Rimer, J. D.; Navrotsky, A.; Banfield, J. F.; Wallace, A. F.; Michel, F. M.; Meldrum, F. C.; Cölfen, H.; Dove, P. M. Crystallization by particle attachment in synthetic, biogenic, and geologic environments. *Science* **2015**, *349* (6247), eaaa6760.

(32) De Stasio, G.; Frazer, B. H.; Gilbert, B.; Richter, K. L.; Valley, J. W. Compensation of charging in X-PEEM: a successful test on mineral inclusions in 4.4 Ga old zircon. *Ultramicroscopy* **2003**, *98* (1), 57–62.

(33) DeVol, R. T.; Metzler, R. A.; Kabalah-Amitai, L.; Pokroy, B.; Politi, Y.; Gal, A.; Addadi, L.; Weiner, S.; Fernandez-Martinez, A.; Demichelis, R.; Gale, J. D.; Ihli, J.; Meldrum, F. C.; Blonsky, A. Z.; Killian, C. E.; Salling, C. B.; Young, A. T.; Marcus, M. A.; Scholl, A.; Doran, A.; Jenkins, C.; Bechtel, H. A.; Gilbert, P. U. P. A. Oxygen spectroscopy and Polarization-dependent Imaging Contrast (PIC)-mapping of calcium carbonate minerals and biominerals. *J. Phys. Chem. B* **2014**, *118* (28), 8449–8457.

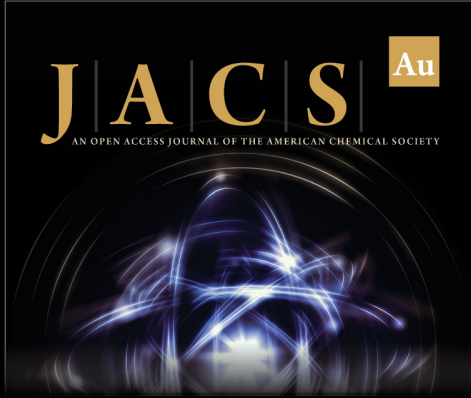
(34) Metzler, R. A.; Zhou, D.; Abrecht, M.; Chiou, J.-W.; Guo, J.; Ariosa, D.; Coppersmith, S. N.; Gilbert, P. U. P. A. Polarization-dependent imaging contrast in abalone shells. *Phys. Rev. B* **2008**, *77*, 064110.

(35) Olson, I. C.; Metzler, R. A.; Tamura, N.; Kunz, M.; Killian, C. E.; Gilbert, P. U. P. A. Crystal lattice tilting in prismatic calcite. *J. Struct. Biol.* **2013**, *183*, 180–190.

(36) Ihli, J.; Wong, W. C.; Noel, E. H.; Kim, Y.-Y.; Kulak, A. N.; Christenson, H. K.; Duer, M. J.; Meldrum, F. C. Dehydration and crystallization of amorphous calcium carbonate in solution and in air. *Nat. Commun.* **2014**, *5* (1), 3169.


(37) GG-Macros, <http://home.physics.wisc.edu/gilbert/software.htm> (accessed 12/17/2021).


(38) DeVol, R. T.; Sun, C.-Y.; Marcus, M. A.; Coppersmith, S. N.; Myneni, S. C. B.; Gilbert, P. U. P. A. Nanoscale transforming mineral phases in fresh nacre. *J. Am. Chem. Soc.* **2015**, *137* (41), 13325–13333.



JACS Au
AN OPEN ACCESS JOURNAL OF THE AMERICAN CHEMICAL SOCIETY

Editor-in-Chief
Prof. Christopher W. Jones
Georgia Institute of Technology, USA

Open for Submissions 

pubs.acs.org/jacsau  ACS Publications
Most Trusted. Most Cited. Most Read.

Supporting information for Faster crystallization during coral skeleton formation correlates with resilience to ocean acidification

Connor A. Schmidt¹, Cayla A. Stifler¹, Emily L. Luffey¹, Benjamin I. Fordyce¹, Asiya Ahmed¹, Gabriela Barreiro Pujol¹, Carolyn P. Breit¹, Sydney S. Davison¹, Connor N. Klaus¹, Isaac J. Koehler¹, Isabelle M. LeCloux¹, Celeo Matute Diaz¹, Catherine M. Nguyen¹, Virginia Quach¹, Jaden S. Sengkhamee¹, Evan J. Walch¹, Max M. Xiong¹, Eric Tambutti², Sylvie Tambutti², Tali Mass³, Pupa U.P.A. Gilbert^{1,4,5*}

¹ Department of Physics, University of Wisconsin, Madison, WI 53706, USA.

² Department of Marine Biology, Centre Scientifique de Monaco, 98000 Monaco, Principality of Monaco.

³ University of Haifa, Marine Biology Department, Mt. Carmel, Haifa 31905, Israel.

⁴ Chemical Sciences Division, Lawrence Berkeley National Laboratory, Berkeley, CA 94720, USA.

⁵ Departments of Chemistry, Materials Science and Engineering, and Geoscience, University of Wisconsin, Madison, WI, 53706, USA.

* Corresponding author: pupa@physics.wisc.edu.

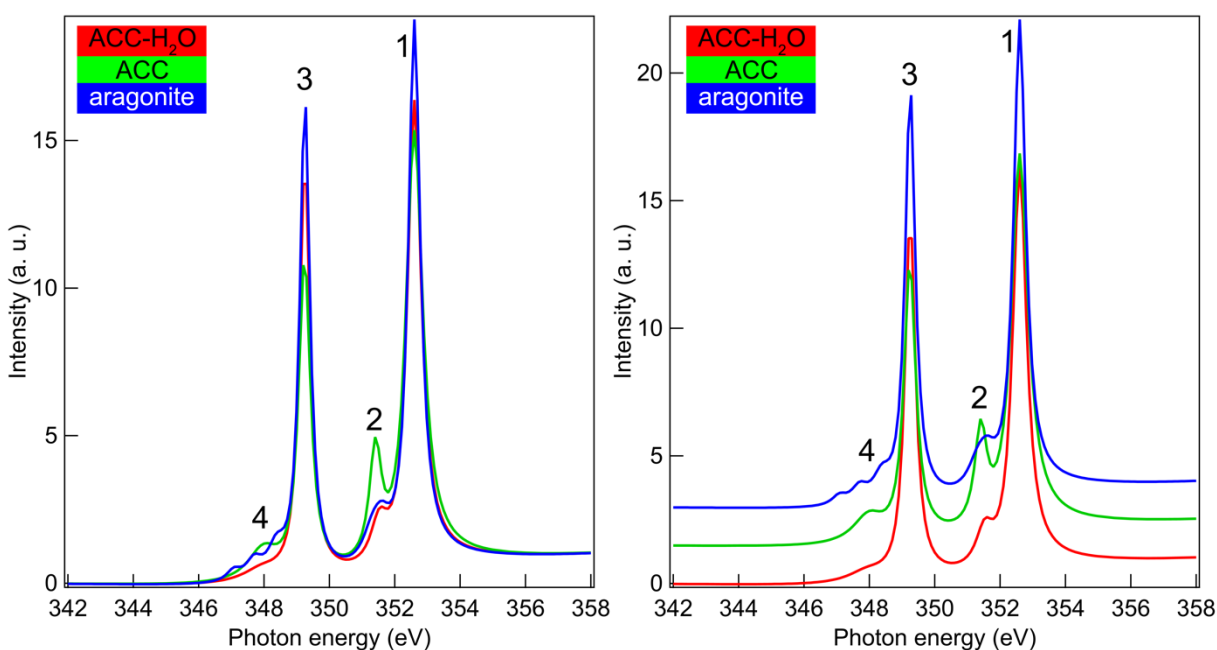


Figure S1. The Cni7 component Ca $L_{2,3}$ -edge spectra, used for all component analyses in this work are presented overlapping (left), and displaced vertically for clarity (right). The aragonite spectrum was obtained by extracting 1441 single pixel spectra from 10 Ca movies, from 2 different coral skeletons, aligning them in energy, averaging them, then peak fitting the average. This strategy was used to eliminate any contributions from noise, both statistical (eliminated by peak fitting) and non-statistical (minimized by using spectra from multiple movies). The ACC-H₂O and ACC spectra were extracted from 60 single pixel spectra from 15 Ca movies, all acquired in regenerating sea urchin spines, and previously used as component spectra in Albéric et al. 2019¹. The 3 spectra were aligned to one another in amplitude and energy between 340 eV and 360 eV, then shifted in energy so the peak 1 was at 352.6 eV, a linear fit to the pre-edge background was subtracted from each of the 3 spectra, and then each spectrum was peak fitted. During peak fitting, 2 arctangents were placed 0.25 eV below peak 3 and peak 1, fixed in position, width, and amplitude, and kept constant for all 3 spectra. Similarly, the background polynomial was fixed and identical for all 3 spectra. These choices were key to obtaining a consistent pre- and post-edge background for all 3 spectra. The results of peak-fitting for the 3 Cni7 component spectra are presented in Table SS. The Cni7 component spectra are included in the Supporting Information as separate .txt files.

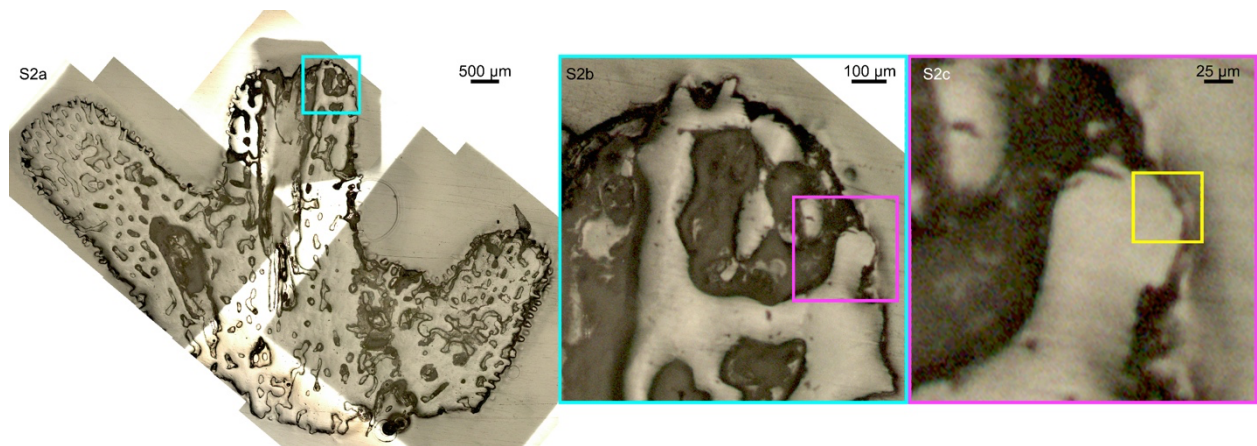


Figure S2. PLM images of the *Acropora* sp. sample. Each colored box indicates where the zoomed-in next image was acquired, with the final yellow box indicating the area of PEEM data acquisition in **Figure 2**.

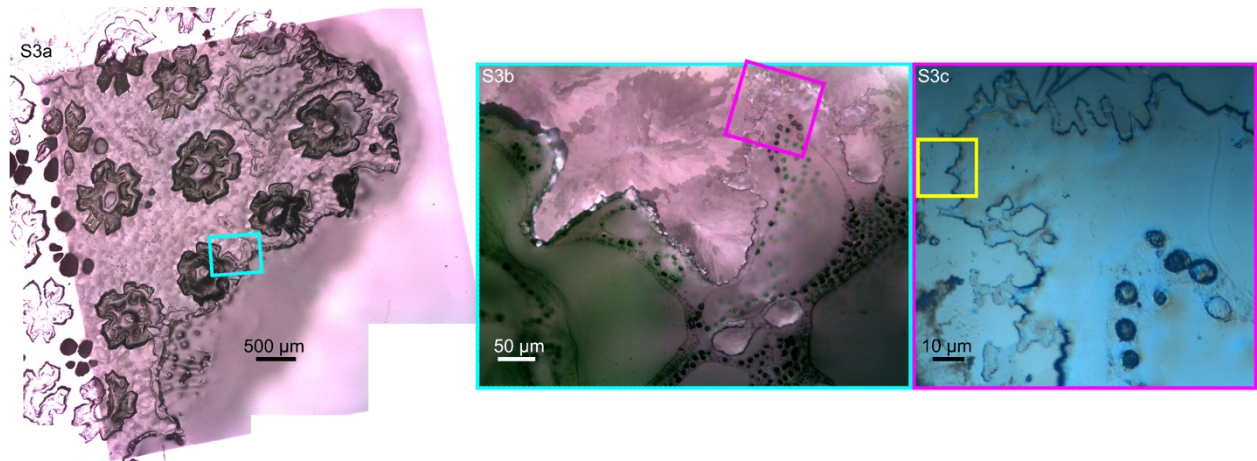


Figure S3. PLM images (**S3a**, **S3b**) and DIC image (**S3c**) of the *Stylophora pistillata* sample. Each colored box indicates where the zoomed-in next image was acquired, with the final yellow box indicating the area of PEEM data acquisition in **Figure 3**.

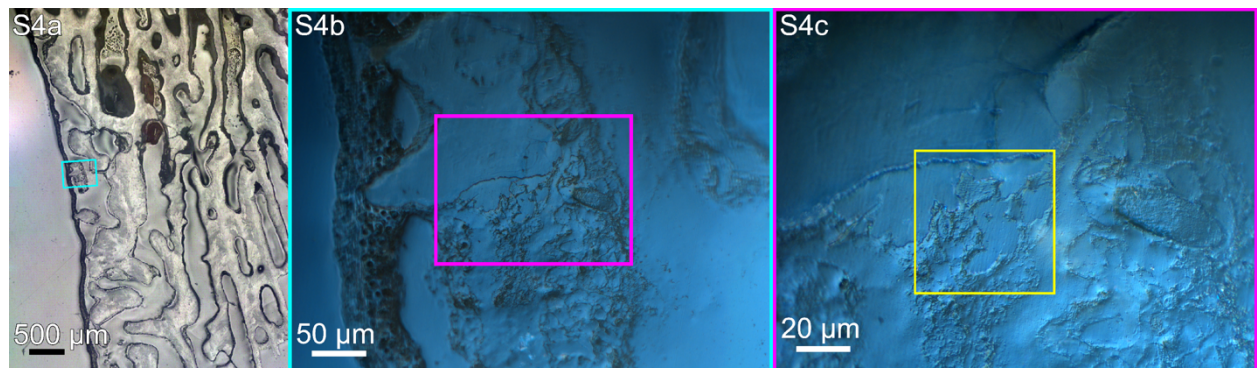


Figure S4. PLM image (**S4a**) and DIC images (**S4b**, **S4c**) of the *Turbinaria peltata* sample. Each colored box indicates where the zoomed-in next image was acquired, with the final yellow box indicating the area of PEEM data acquisition in **Figure 4**.

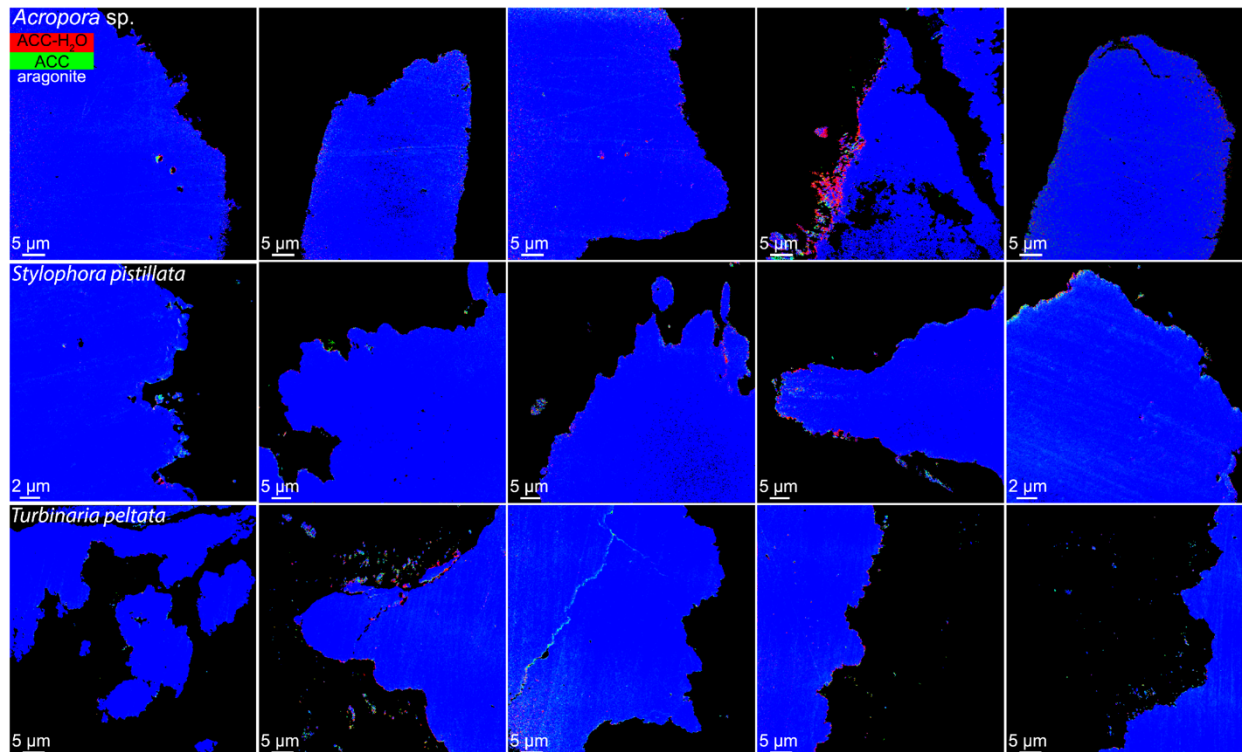


Figure S5. Component maps for each area analyzed in **Tables S1-S4**, including those shown in **Figures 2,3,4** on the left. Five areas from *Acropora*, *Stylophora*, and *Turbinaria* are presented in the top row, the middle, and the bottom row, respectively.

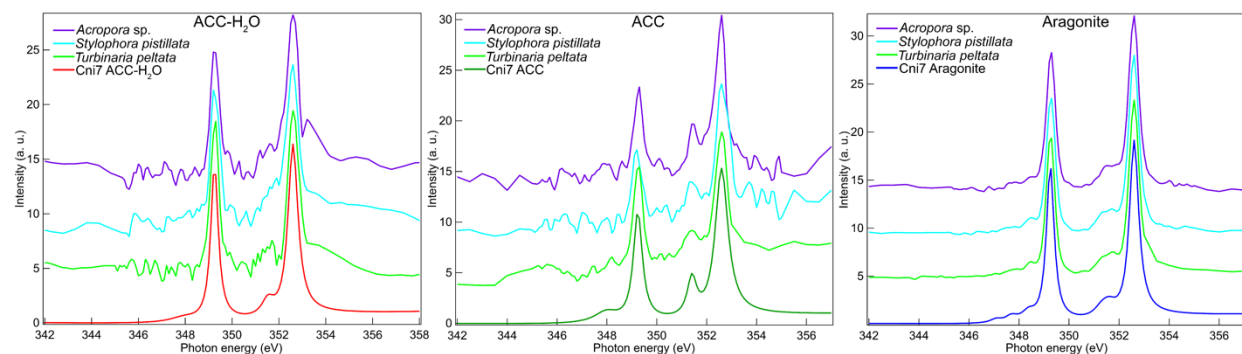


Figure S6. Single-pixel Ca L_{2,3}-edge ACC-H₂O, ACC, and aragonite spectra extracted from one of the areas shown in **Figures 2,3,4** (top 3 spectra in each panel), and the ACC-H₂O, ACC, and aragonite spectrum from the Cni7 component spectra (bottom spectrum). Pixels are 60 nm for *Acropora* and *Turbinaria* data, 20 nm for *Stylophora* data. The selected single-pixel spectra contained over 90% ACC-H₂O, or ACC, or aragonite, as identified by best-fitting in component mapping. The spectra are displaced vertically for clarity. Spectra from amorphous phases tend to have lower intensity than crystalline ones, leading to spectra with more pronounced noise. This makes sense, as ACC-H₂O has lower Ca density than ACC, and much lower than aragonite.

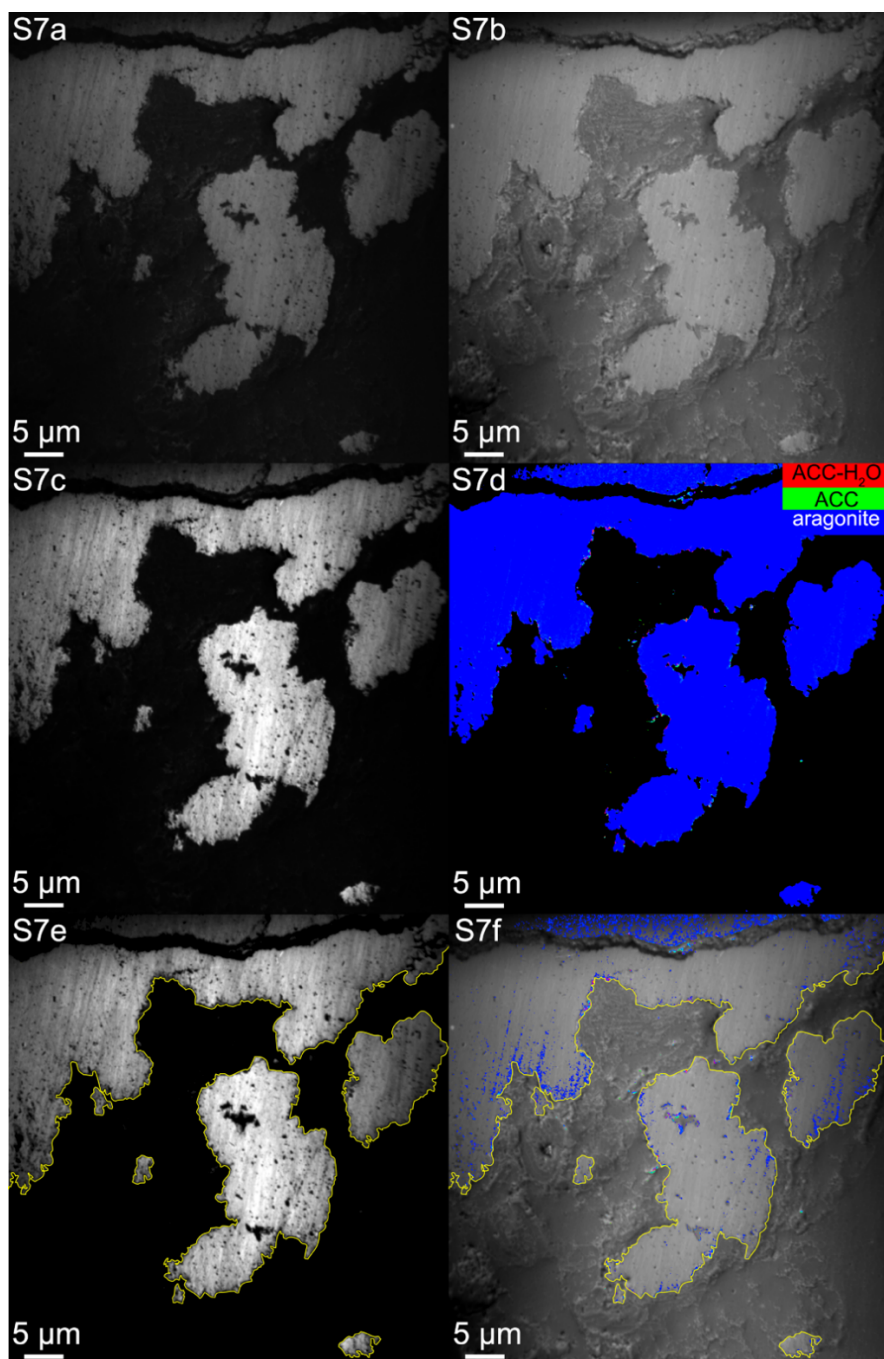


Figure S7. *S7a.* PEEM single image, taken on peak 1 at 352.6 eV (*Fig. S1* shows peak numbers). *S7b.* Average image, obtained by digitally averaging all 121 PEEM images in a Ca stack. *S7c.* A Ca concentration map obtained by digital subtraction of images on-peak and off-peak. The on-peak image is the average of 5 images, 1 acquired at the 352.6 eV peak and 4 at ± 0.1 and ± 0.2 eV from peak, the off-peak image is the average of 9 images acquired at and around 344 eV. *S7d.* A component map, masked using all 3 masks, the difference mask, the χ^2 mask, and the manual mask eliminating spurious single-pixels in the epoxy or tissue. *S7e.* The same Ca map in *S7c*, overlaid with the black mask used in component mapping, and the yellow line outlining the skeleton. The yellow line was produced by outlining the black mask in *S7d*, in Adobe Photoshop®, using the “stroke” tool, after selecting only the contiguous skeleton and other skeletal regions not connected in this 2D polished cross-section, presumably connected in 3D, and $>2 \mu\text{m}$. *S7f.* Average PEEM image, overlaid with the yellow line defined in *S7e*, and part of the component map in *S7d*, where all epoxy black pixels and aragonite blue pixels were removed, using the Adobe Photoshop® “magic wand” tool, with a tolerance of 26, to retain all amorphous pixels, and eliminate all crystalline or epoxy pixels. This region’s component map, mask, and yellow outline were obtained with precisely the same methods as all others presented in *Figures 2d,3d,4d*, which are analogous to the panel *S7f* here.

Table S1

genus	total extra-skeletal volume analyzed (μm^3)	# extra-skeletal particles observed	density of extra-skeletal particles (#particles/ μm^3)	average density of extra-skeletal particles	standard deviation
<i>Acropora</i>	5.19	3	0.6	4.0	2.3
	2.43	8	3.3		
	2.62	8	3.1		
	4.53	32	7.1		
	3.98	23	5.8		
<i>Stylophora</i>	0.58	13	22.5	11.9	11.9
	4.22	15	3.6		
	5.46	8	1.5		
	6.93	14	2.0		
	0.47	14	29.8		
<i>Turbinaria</i>	5.31	18	3.4	11.9	10.5
	5.47	160	29.3		
	5.85	40	6.8		
	6.97	128	18.4		
	2.67	4	1.5		

Table S1. Extra-skeletal particle density. Results from counting the number of particles observed in each area, divided by the total volume of extra-skeletal space analyzed in each area by PEEM with component mapping. Extra-skeletal particles are defined for this purpose as any group of 4 or more contiguous unmasked pixels outside of the skeleton. Extra-skeletal volume analyzed is obtained by the measuring the number of pixels outside the skeleton, converting that into an area in μm^2 , and multiplying it by the $0.003 \mu\text{m}$ thickness of probed with component mapping. *Stylophora* and *Turbinaria* have areas of high- and low-density of extra-skeletal particles, giving rise to the larger standard deviation measured.

Table S2

genus	total # pixels intra-skeletal, not masked	# ACC-H ₂ O intra-skeletal pixels	# ACC intra-skeletal pixels	% intra-skeletal amorphous pixels	% intra-skeletal crystalline pixels	average % intra-skeletal amorphous pixels	standard deviation
<i>Acropora</i>	65200	4416	6378	16.6	83.4	23.9	9.2
	93936	8395	19086	29.3	70.7		
	75819	5820	6228	15.9	84.1		
	153553	20980	10230	20.3	79.7		
	110387	13555	27626	37.3	62.7		
<i>Stylophora</i>	151682	2855	11890	9.7	90.3	15.0	6.6
	113654	2768	5481	7.3	92.7		
	99257	6778	9600	16.5	83.5		
	92290	6528	9535	17.4	82.6		
	175832	8103	33889	23.9	76.1		
<i>Turbinaria</i>	190544	1645	4273	3.1	96.9	12.2	5.7
	95267	6065	8989	15.8	84.2		
	79155	1137	7990	11.5	88.5		
	59335	3760	6918	18.0	82.0		
	68317	1201	7419	12.6	87.4		

Table S2. Intra-skeletal percentages of amorphous pixels. Results from counting the number of (#) amorphous pixels in the surface 2 μ m-thick band of all coral areas analyzed. The # pixels were counted in Adobe Photoshop® as described in the Methods. Only pixels with $\geq 10\%$ of the relevant phase were counted for each amorphous phase. Crystalline pixels were those with $>90\%$ aragonite. In the first row of each genus are the data presented in Figures 2,3,4, and in following rows are data from other areas in the genus. Different total pixel counts arise from different fields of view and different amounts of skeletal surface area, so the % amorphous pixels is the most important number. The last two columns show the average % amorphous pixels and the standard deviation for each genus.

Table S3

genus	total # pixels extra-skeletal, not masked	# ACC-H ₂ O extra-skeletal pixels	# ACC extra-skeletal pixels	% extra-skeletal amorphous pixels	% extra-skeletal crystalline pixels	average % extra-skeletal amorphous pixels ± StDev	average % 1- μ m-skeleton surface amorphous pixels ± StDev	significant?
<i>Acropora</i>	1021	192	176	36.0	74.0	63.0 ± 22.8	28.9 ± 10.0	yes p=0.075
	364	93	74	45.9	54.1			
	18977	8095	6865	78.8	21.2			
	1039	388	561	91.3	8.7			
<i>Stylophora</i>	3160	609	1922	80.1	19.9	91.2 ± 8.4	23.7 ± 9.1	yes p=0.000047
	956	373	636	100	0.0			
	2751	1016	1536	92.8	7.2			
	1698	651	816	86.4	13.6			
	1415	538	749	91.0	9.0			
<i>Turbinaria</i>	700	133	312	63.6	36.4	81.9 ± 11.1	18.8 ± 8.6	yes p=0.00032
	14305	5438	7584	91.0	9.0			
	1533	500	888	90.5	9.5			
	4129	900	2503	82.4	17.6			

Table S3. Extra-skeletal percentages of amorphous pixels. Results from counting the number of (#) amorphous pixels in particles outside the skeleton in all coral areas analyzed, except for one area of *Acropora* and one area of *Turbinaria* that did not contain any extra-skeletal particles. As in **Table S2**, only pixels with $\geq 10\%$ of the relevant phase were counted for each amorphous phase. Crystalline pixels were those with $>90\%$ aragonite. Again, in the first row of each genus are the data presented in **Figures 2,3,4**, and in following rows are data from other areas in the genus. Again, different total pixel counts arise from different fields of view and different amounts of extra-skeletal particles, so the % amorphous pixels is the most important number. The % of amorphous pixels can be over 100% because ACC and ACC-H₂O are counted separately, thus, if a pixel has both $>10\%$ ACC-H₂O $>10\%$ ACC it is counted twice. This only occurred in one area, which had 100.6%, and was manually adjusted to 100% amorphous and 0% crystalline, which are physically realistic numbers.

For comparison, in the second to last column we included the % amorphous pixels detected in the outermost 1 μ m layer of the skeleton, termed “skeleton surface”, which contains the greatest % amorphous pixels compared with any other part of the skeleton. The extra-skeletal particles contain a significantly higher % of amorphous pixels than the most amorphous skeleton surface. The significance and corresponding p-values are indicated in the last column. P-values listed were calculated using a 2-sample t-test, without assuming equal variances.

Table S4

genus	Depth in coral skeleton (μm)	% amorphous pixels in A194	% amorphous pixels in A192	% amorphous pixels in A202	% amorphous pixels in A196	% amorphous pixels in A200	avg % amorphous pixels in 5 areas	standard deviation across 5 areas
<i>Acropora</i>	0.11	33.4	52.0	68.3	37.2	51.9	48.5	13.9
	0.26	27.6	47.8	58.5	30.1	47.2	42.2	13.1
	0.53	24.4	42.4	52.0	24.4	38.6	36.4	12.0
	1	21.3	36.4	45.3	20.3	28.9	30.4	10.6
	2	16.6	29.3	37.3	15.9	20.3	23.9	9.2
	4	12.0	21.7	29.3	12.2	16.3	18.3	7.3
<i>Stylophora</i>	Depth in coral skeleton (μm)	% amorphous pixels in S146	% amorphous pixels in S01	% amorphous pixels in S11	% amorphous pixels in S15	% amorphous pixels in S99	avg % amorphous pixels in 5 areas	standard deviation across 5 areas
	0.125	31.5	33.4	47.3	58.1	66.2	47.3	15.1
	0.25	29.8	27.4	42.0	50.9	61.8	42.4	14.4
	0.5	24.7	19.1	33.9	40.4	53.1	34.2	13.3
	1	16.9	11.8	24.2	27.5	38.1	23.7	10.2
	2	9.7	7.3	16.5	17.4	23.9	15.0	6.6
	4	5.6	4.8	11.5	11.3	15.7	9.8	4.5
<i>Turbinaria</i>	Depth in coral skeleton (μm)	% amorphous pixels in T35	% amorphous pixels in T31	% amorphous pixels in T37	% amorphous pixels in T61	% amorphous pixels in T63	avg % amorphous pixels in 5 areas	standard deviation across 5 areas
	0.16	22.9	54.2	32.1	73.6	40.5	44.7	19.8
	0.27	12.8	44.1	33.4	66.3	32.9	37.9	19.5
	0.5	8.5	32.4	24.4	43.3	25.7	26.9	12.7
	1	5.2	22.6	17.3	28.7	18.7	18.5	8.6
	2	3.1	15.9	11.5	18.0	12.6	12.2	5.7
	4	2.2	11.3	8.9	11.5	9.6	8.7	3.8

Table S4. Intra-skeletal percentages of amorphous pixels vs. distance from surface. Results from counting the percentage of (%) pixels amorphous pixels (either ACCH₂O or ACC) within the skeleton surface, at various distances from the surface, indicated by a dotted line in Figures 2,3,4. Each genus was measured in quintuplicate, and all data are averaged over the 5 areas in the last column. These data decay logarithmically, as shown in Figure 5.

Table S5

Fit parameters	ACC-H ₂ O	ACC	Aragonite
p0	-0.22154	-0.22154	-0.22154
p1	-0.017219	-0.017219	-0.017219
p2	0.0021331	0.0021331	0.0021331
p3	0.00020401	0.00020401	0.00020401
pk1 Lorentzian Amplitude	12.411	14.14	12.617
<i>pk1 position</i>	<i>352.6</i>	<i>352.6</i>	<i>352.6</i>
Width	0.51202	0.62488	0.4439
pk2 Lorentzian Amplitude	1.55	2.7	1.35
<i>pk2 position</i>	<i>351.53</i>	<i>351.41</i>	<i>351.6</i>
Width	0.65	0.45	0.7
pk3 Lorentzian Amplitude			1
<i>pk2' position</i>			<i>351.3</i>
Width			0.7
pk4 Lorentzian Amplitude	8.5172	7.2712	9.3555
<i>pk3 position</i>	<i>349.25</i>	<i>349.24</i>	<i>349.25</i>
Width	0.38397	0.4326	0.36859
pk5 Lorentzian Amplitude	1.1156	2.0779	1
<i>pk4 position</i>	<i>347.95</i>	<i>347.98</i>	<i>348.38</i>
Width	0.2	1.1895	0.65
pk6 Lorentzian Amplitude			0.6
<i>pk4' position</i>			<i>347.7</i>
Width			0.6
pk7 Lorentzian Amplitude			0.3
<i>pk4'' position</i>			<i>347.08</i>
Width			0.5322
AT1 Arc-Tangent Amplitude	0.3	0.3	0.3
<i>AT1 position</i>	<i>349</i>	<i>349</i>	<i>349</i>
Width	0.2	0.2	0.2
AT2 Arc-Tangent Amplitude	0.8	0.8	0.8
<i>AT2 position</i>	<i>352.35</i>	<i>352.35</i>	<i>352.35</i>
Width	0.2	0.2	0.2

Table S5. Component spectra peak-fitting parameters. Cni7 Fit parameters used in peak-fitting the Cni7 component spectra. Values in **bold** were held, that is, not allowed to change during peak fitting in Igor Pro Carbon® using GG Macros³. *Red italics* font indicates energy-positions. Aragonite required the use of several more Lorentzian curves than ACC-H₂O or ACC, so some rows are blank for the amorphous phases. Abbreviations: pk = peak, AT = arctan.

Supporting references

1. Albéric, M.; Stifler, C. A.; Zou, Z.; Sun, C.-Y.; Killian, C. E.; Valencia, S.; Mawass, M.-A.; Bertinetti, L.; Gilbert, P. U. P. A.; Politi, Y., Growth and regrowth of adult sea urchin spines involve hydrated and anhydrous amorphous calcium carbonate precursors. *Journal of Structural Biology: X* **2019**, *1*, 100004.
2. GG-Macros, <http://home.physics.wisc.edu/gilbert/software.htm> **2021**.